SAND2019-13994C

Hydrocarbon and Water Desorption from Iron-Oxide Surfaces using Molecular Dynamics

Jason P. Koski[a)] and J. Matthew D. Lane

Sandia National Laboratories, P.O. Box 5800, Albuquerque, New Mexico 87185

[a)]*Electronic mail: jkoski@sandia.gov*

Abstract. The high-rate desorption of hydrocarbons, water, and hydrocarbon-water mixtures was investigated using classical molecular dynamics. The fundamental and mechanistic understanding of molecular desorption from metal oxide surfaces is important to understand the current loss in pulse power machines. We analyze the desorption as a function of hydrocarbon architecture, coverage, chain length, and the composition of hydrocarbon-water mixtures. We find that for the temperature ramp rates tested, that branched naphthene hydrocarbons exhibit similar desorption trends as linear paraffin hydrocarbons. Furthermore, the hydrocarbon desorption is independent of surface coverage on the substrate. However, the desorption temperature decreases significantly as a function of hydrocarbon chain length. We find that in the case of mixtures, water adsorbs to the substrate and hydrocarbons sit atop the water at 300 K. The desorption temperature changes minimally for both hydrocarbons and water as a function of varying hydrocarbon concentration. On the contrary, the hydrocarbon structure is strongly dependent on the water coverage and can affect the desorption significantly if the temperature ramp rate is extremely fast. Varying the water concentration has a substantially less effect on the hydrocarbon desorption when the temperature ramp rate is relatively slow.

INTRODUCTION

A prominent issue in Sandia National Laboratories' Z-machine is the observed current loss within the magnetically insulated transmission lines (MITLs) that deliver the electromagnetic energy to the central experiment [1, 2]. A known source of the current loss is the plasma that forms in the MITLs, which shunts the current as it is delivered to load. The present understanding of this plasma formation is from the Ohmic heating that causes insulating molecules on the surface of the electrodes to desorb and ionize. This Ohmic heating is extremely rapid, reaching temperatures above 1300 K in just 100s of ns. As such, a fundamental and mechanistic understanding of this molecular desorption will improve the efficiency and design of next-generation pulse power machines.

Currently, state-of-the-art plasma codes [1, 3, 4] are used to model the relatively large-scale plasma formation and ensuing dielectric breakdown in these systems. A key aspect to these codes is that they rely on accurate predictions of molecular composition and desorption rate from electrode surfaces. While *ab initio* [5, 6, 7, 8], reactive molecular dynamics [9], and classical molecular dynamics [10, 11, 12] studies have modeled the interaction of molecules with steel-like surfaces, they focus on the adsorption energy to the surface or the structure of the molecules on the surface at ambient conditions. Previous work that models the Z-machine environment focused on the desorption of water from metal oxide surfaces using a combination of density functional theory (DFT), grand canonical Monte Carlo (GCMC), and classical molecular dynamics (MD) [13]. However, the presence of mineral oil in the Z-machine suggests that hydrocarbons are present on the electrode surfaces.

In this paper, we analyze the temperature-induced desorption of hydrocarbons and hydrocarbon/water mixtures from a Fe_2O_3 (0 0 0 1) surface at rates comparable to the Z-machine using classical MD. We first analyze the importance of hydrocarbon structure on the desorption rate by comparing simulations containing branched naphthene hydrocarbons versus linear paraffin hydrocarbons. Next we look at the effect of both hydrocarbon coverage and chain length in the hydrocarbon desorption. Finally, we analyze the desorption of hydrocarbon/water mixtures with varying compositions to assess how the presence of hydrocarbons affect the water desorption and vice versa.

METHODOLOGY

Figure 1 shows visualizations and the associated color scheme of the components used in this study. The α-Fe_2O_3 (0 0 0 1) substrate was modeled using ClayFF [14], the hydrocarbons using OPLS [15], and the water using a SPC model [16]. All MD simulations were carried out in Sandia's LAMMPS code [17] using a lj/cut/coul/long pair_style with a 9 Å cutoff and pppm k_space style with a 1e-4 threshold. As described in Lane *et al.* [13], dipole corrections were applied using the kspace_modify slab option built into LAMMPS. Here, we use the same parameters as in Lane *et al.* to treat the substrate, water, and substrate-water interactions. The original OPLS parameters of Jorgensen *et al.*

[15] are used to treat the hydrocarbons with the exception of the partial charges reflecting the more recent work of Siu *et al.* [18]. Arithmetic mixing rules were used to calculate the cross-terms between the substrate and water while geometric mixing rules were used to calculate the hydrocarbon-substrate and hydrocarbon-water cross-terms. A 1.0 fs timestep was used in all simulations.

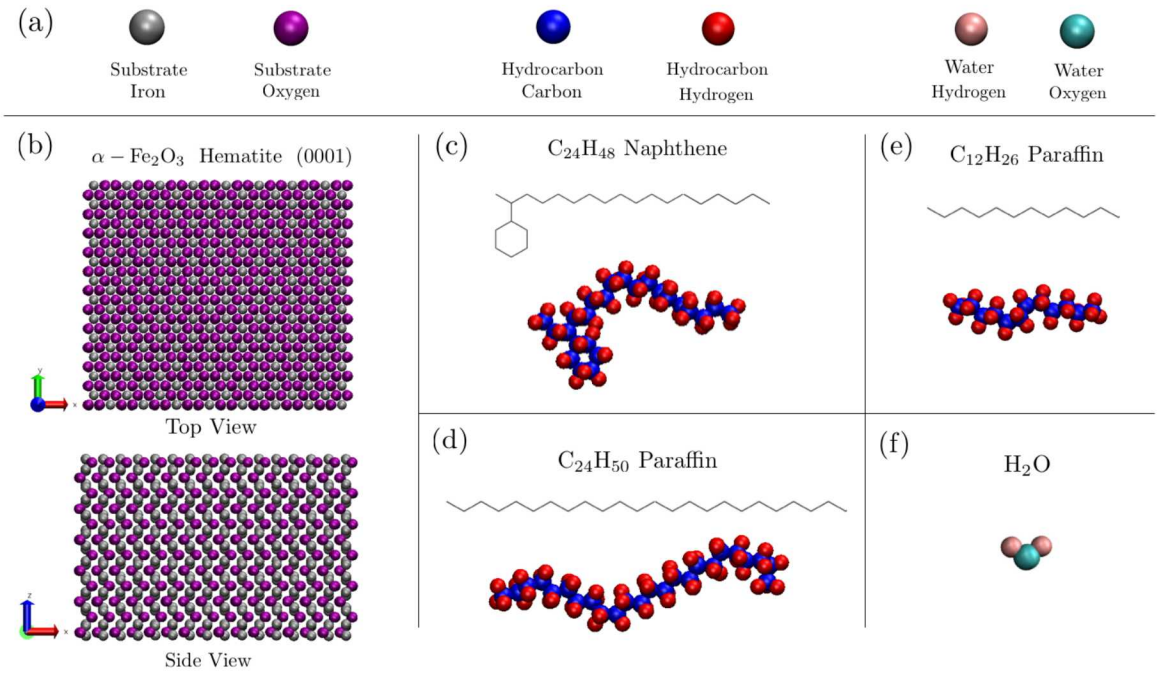

FIGURE 1. (a) Color scheme used to represent the different atoms in this study. (b) Top and side view of the α-Fe_2O_3 (0 0 0 1) substrate. Schematic and atomistic representations of (c) $C_{24}H_{48}$ naphthene, (d) $C_{24}H_{50}$ paraffin, (e) $C_{12}H_{26}$ paraffin, and (f) water. Note that the naphthene and paraffin molecules are synonymously referred to as branched and linear hydrocarbons, respectively.

With the exception of the results shown in Figure 2 (described below), all simulations were run using a fix nve for the hydrocarbons and water while the substrate was treated with a fix npt with a thermal damping coefficient of 100 fs. The length in the x- and y-directions were allowed to fluctuate with a target pressure of 0 and pressure damping coefficient of 5000 fs. A fix_modify command was used in junction with a compute temp command to adjust the temperature of the substrate. This was to ensure that the substrate temperature reflected the temperature of only the substrate atoms and not from the hydrocarbons and/or water. Unless otherwise specified, each temperature ramp simulation was preceded by a equilibration simulations at 300 K for 0.5 ns. Equilibration was monitored by assessing the distance of the hydrocarbons and/or water from the substrate had equilibrated and from visual observation. In some of the hydrocarbon/water mixtures (described further in the Results section), additional equilibration time was needed due to the hydrocarbons phase separating into droplets on top of the water. The temperature ramps were then conducted at rates of 2000 K/ns, 200 K/ns, and in some cases, 50 K/ns.

Figure 2 shows snapshots of simulations used to inform the hydrocarbon initialization of the production desorption runs. The top row shows the initial placement of 4 $C_{24}H_{50}$ paraffin chains while the bottom row shows the same chains after 1 ns. All trials were run using a frozen substrate and a Langevin thermostat for the hydrocarbons at 300 K. A total of 30 trials were run; 10 trials for each ϕ_0 = 0°, 45°, and 90°, where ϕ_0 is defined as the initial radial angle between the x-axis and the chain orientation. In each of the 10 trials, the 4 $C_{24}H_{50}$ paraffin chains were shifted 0.5 Å in the direction perpendicular to the long-axis of the chain to account for any possible angular or translational preference of the chains with respect to the substrate. Note that with respect to the iron atoms in the top row of the substrate (shown in silver), multiples of 60° are redundant. In every trial, the long axis of the chains align with ϕ = 0°, 60°, or 120° after $\approx$ 0.3 ns and remains in that orientation up until the final simulation time of 1 ns. The ends of the chains on the outside of the rafts are observed to fluctuate from the primary orientation of the raft indicating the thermal energy in these parts of the raft is greater than the hydrocarbon-hydrocarbon side-by-side interaction as well as the hydrocarbon-substrate interaction.

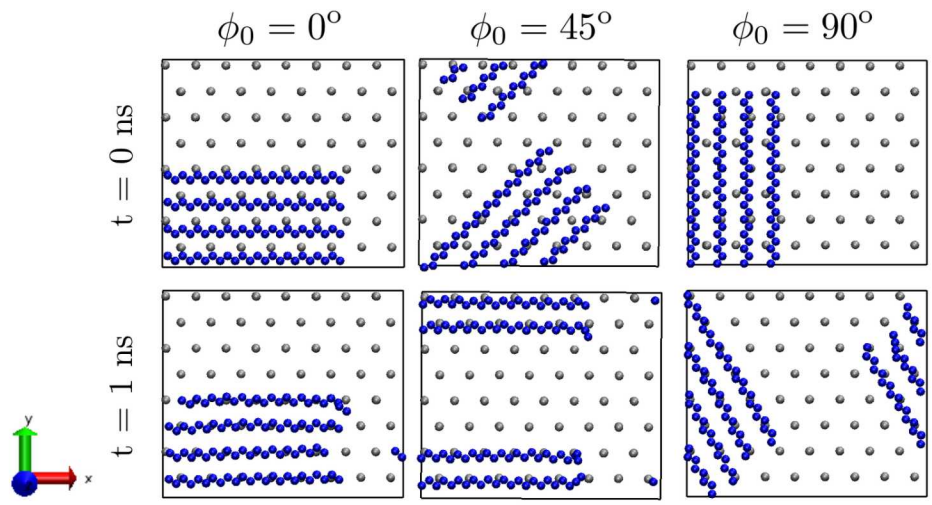

FIGURE 2. Bird's-eye visualization demonstrating preferred orientation of polymer 'rafts' (rafts meaning polymer chains lined up side-by-side) on top of the α-Fe_2O_3 (0 0 0 1) substrate. The top row shows the initial placement of 4 $C_{24}H_{50}$ paraffin chains while the bottom row shows the same chains after 1 ns. Here, ϕ_0 is defined as the initial radial angle between the x-axis and the chain orientation. All trials were run at 300 K. Only the top row of the iron atoms (silver) and the carbons (blue) are shown to emphasize the preference of the carbons within the hydrocarbons to maximize contact with the uppermost iron atoms.

Fig. 2 demonstrates the preference of the carbons within the hydrocarbons to maximize contact with the uppermost iron atoms, which corresponds to the long-axis of the chains aligning with ϕ = 0^o (the x-axis). As such, the long-axis of the hydrocarbons were oriented along the x-axis while minimizing the end-to-end distance between chains. The side-to-side distance was determined from placing each hydrocarbon over a row of the uppermost irons within the substrate. The side-to-side distance between chains multiplied by the end-to-end distance (including the distance between head-to-head groups of neighboring chains) was used to calculate an area per chain. To define a coverage, θ, for the hydrocarbons, we then used the number of chains and divided that by the chain per area multiplied by the area of the substrate. For the initialization of the hydrocarbon-water mixtures, preliminary simulations showed that if the water was placed on top of the hydrocarbons, the water would diffuse to the substrate and the hydrocarbons would then sit on top of the water in as short as 0.25 ns. Subsequent simulations were then initialized by placing the water directly on the substrate and the hydrocarbons 2.8 Å above the water. The water was initialized in the same manner as described in Lane *et al.*. In all production desorption simulations, the substrate shown in Fig. 1 (~4.1 nm x ~3.6 nm x ~3 nm, containing 3840 atoms) was replicated 12 and 9 times in the x- and y-directions, respectively.

Finally, we considered a hydrocarbon desorbed if every carbon was greater than 20 Å above the substrate and a water molecule was desorbed if the water's oxygen was greater than 20 Å above the substrate. We removed a molecule from the system if any part of the molecule was greater than ~121.7 Å above the substrate.

RESULTS

Figure 3 looks at a comparison of the molecular desorption between linear alkane, or paraffin, hydrocarbons ($C_{24}H_{50}$) and branched cycloalkane, or naphthene, hydrocarbons ($C_{24}H_{48}$). The number of hydrocarbon chains initially each system is 648. Figure 3 demonstrates that the desorption of each chain architecture for a given temperature ramp rate is extremely similar. If we look at the temperature associated when θ = (1/2)θ_0, where θ_0 is the initial coverage, for 2000 K/ns, T $\approx$ 859.0 K and 872.0 K for the paraffin and naphthene hydrocarbons, respectively, while for 200 K/ns, T $\approx$ 587.3 and 576.5 for the paraffin and naphthene hydrocarbons, respectively. These temperatures equate to just a 1.5%-2.0% difference. This result indicates that for this chain length and these temperature ramp rates, the differences in the desorption are small. As such, the rest of the paper focuses on linear paraffin chains to most simply analyze the effect of hydrocarbon coverage and chain length.

Figure 4 shows desorption profiles for $C_{24}H_{50}$ paraffin hydrocarbons with varying coverages. The two figures show

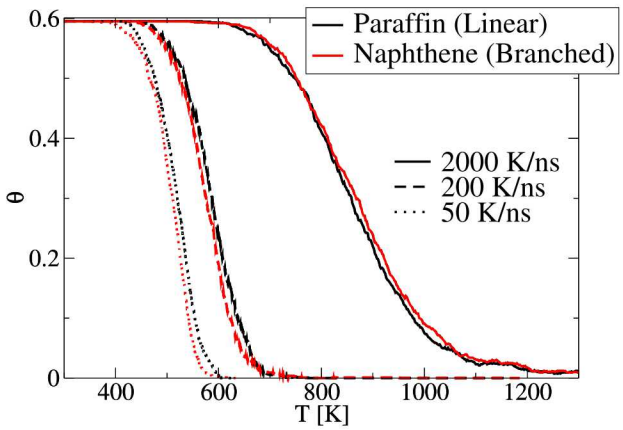

FIGURE 3. Desorption profiles for paraffin (black) and naphthene (red) hydrocarbons with different temperature ramp rates; 2000 K/ns (solid), 200 K/ns (dashed), and 50 K/ns (dotted). In each system, there are 648 hydrocarbons with 24 carbons per molecule.

the same data but presented in two different ways. The left figure shows coverage as a function of temperature while the right figure shows the fraction of initial chains on the surface as a function of temperature. This data shows that the hydrocarbon desorption is largely independent of coverage. When the desorption profiles are plotted with the fraction of initial chains on the surface, the desorption profiles fall on top of one another. This result is very different from what is observed in the desorption of water [13], where the desorption rate of water was shown to be directly linked to the water coverage. While the left figure shows the hydrocarbon desorption having three distinct curves (*i.e.* three distinct desorption temperatures) for a given θ, water was shown to have the same desorption temperature for a given θ.

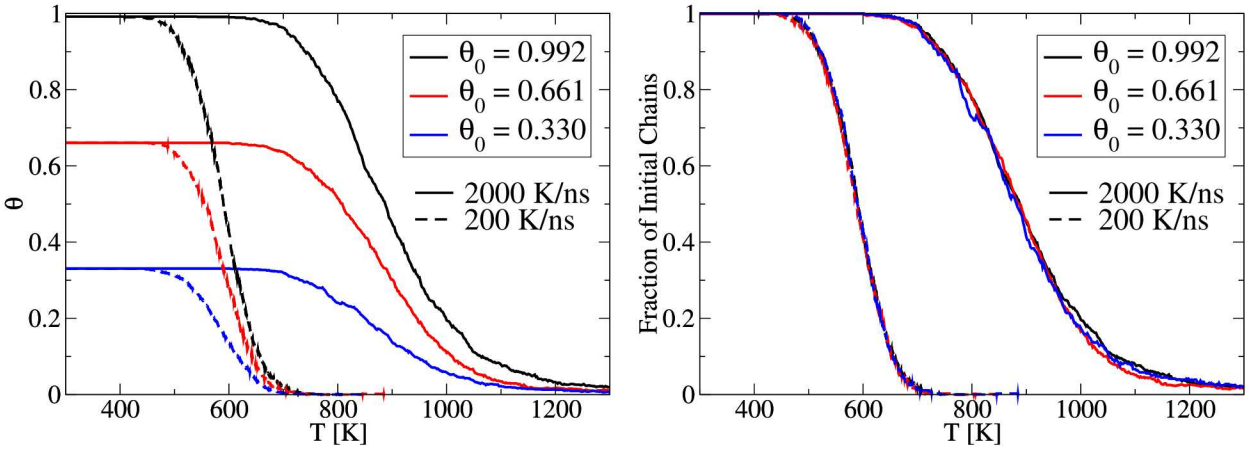

FIGURE 4. Desorption profiles for varying coverages of $C_{24}H_{50}$ paraffin hydrocarbons, (black) $\theta_0 = 0.992$, (red) $\theta_0 = 0.661$, and (blue) $\theta_0 = 0.330$, with different temperature ramp rates; (solid) 2000 K/ns and (dashed) 200 K/ns. The left and right figures show the same data but presented in different ways. The left figure shows coverage as a function of temperature while the right figure shows the fraction of initial chains as a function of temperature. The black, red, and blue curves correspond to systems with 1080, 720, and 360 chains initially on the surface.

Figure 5 shows desorption profiles for paraffin hydrocarbons of varying length; $C_{24}H_{50}$ and $C_{12}H_{26}$. In each system, the number of carbons are held constant at 25,920 (1080 $C_{24}H_{50}$ chains and 2160 $C_{12}H_{26}$ chains). Figure 5 demonstrates that as the chain length is increased, the desorption temperature increases for both temperature ramp rates. Generally, the hydrocarbons have attractive van der Waals forces to the substrate. As the chain length is increased, the effective strength of the van der Waals interaction increases due to the increased number of carbons and hydrogens in

the molecule.

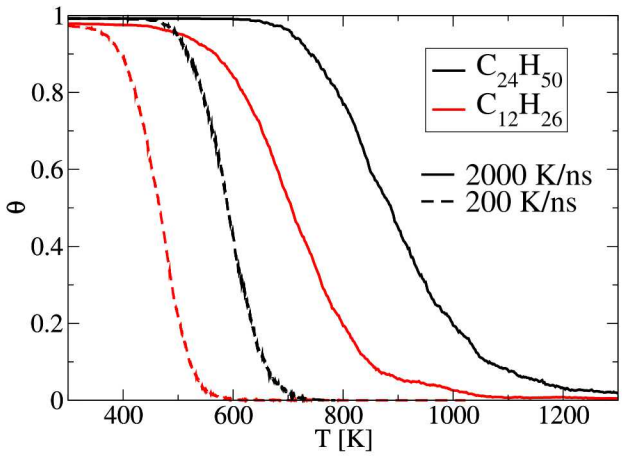

FIGURE 5. Desorption profiles for polyethylene hydrocarbons of varying length, (black) $C_{24}H_{50}$, (red) $C_{12}H_{26}$ with different temperature ramp rates; (solid) 2000 K/ns and (dashed) 200 K/ns.

Next, we focus on hydrocarbon-water mixtures. Figure 6 looks at both the hydrocarbon and water desorption as a function of varying hydrocarbon concentration sitting atop a full monolayer of water. For both 2000 K/ns and 200 K/ns, the varying hydrocarbon concentration has overall little effect on the overall desorption. At both temperature ramp rates, the hydrocarbons desorb much more quickly than the water despite sitting atop the water. This indicates that the conduction of heat to the hydrocarbons through the water is a relatively fast process and that the binding energy of the water to the substrate is much greater than the binding energy of the hydrocarbon to the water. The hydrocarbon desorption temperature for when $\theta = (1/2)\theta_0$ is less than 2.5% different across all coverages for a given temperature ramp rate. The water desorption is also minimally affected by the varying hydrocarbon concentration. The desorption temperature for when $\theta = (1/2)\theta_0$ at the highest hydrocarbon concentration is only ~3.5% higher than when no hydrocarbons are present. The reduction is the desorption temperature can be attributed to the increased crowdedness of the chains as the water is desorbing from the surface though once again, the hydrocarbons desorb much more quickly than the water. This corresponds to the water desorption curves being the most different at lower temperatures and converging at higher temperatures.

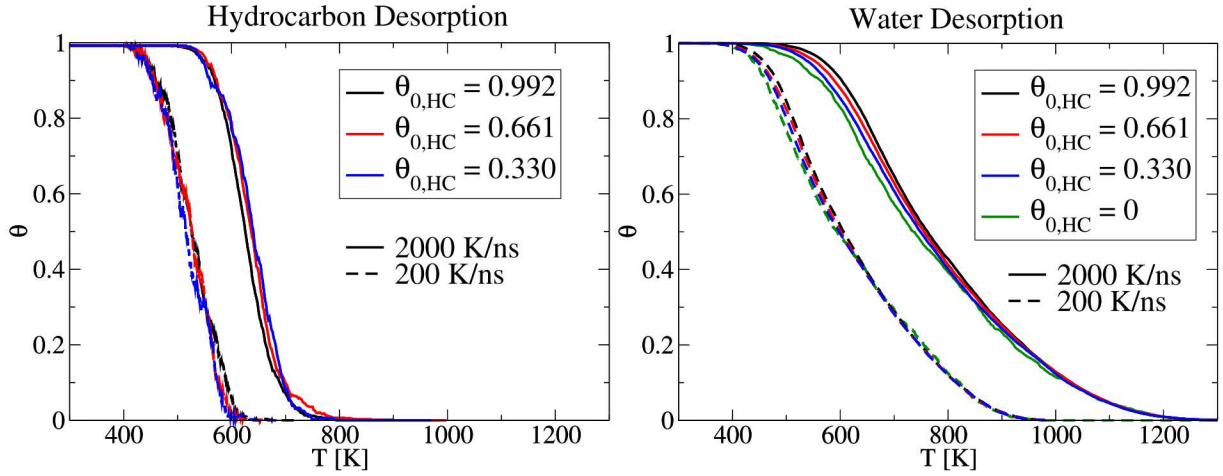

FIGURE 6. Desorption profiles for hydrocarbon-water mixtures with varying hydrocarbon concentration, (black) $\theta_{0,HC} = 0.992$, (red) $\theta_{0,HC} = 0.661$, (blue) $\theta_{0,HC} = 0.330$, and (green) $\theta_{0,HC} = 0$. with different temperature ramp rates; (solid) 2000 K/ns and (dashed) 200 K/ns. The left figure shows the hydrocarbon desorption while the right figure shows the water desorption. The green curve is omitted from the left figure because there is no hydrocarbons in that system. The same color/line-types correspond to the same simulation.

Figure 7 looks at both the hydrocarbon and water desorption as a function of varying water concentration sitting beneath a $\theta = 0.992$ coverage of hydrocarbons. Importantly, as these systems equilibrated, the hydrocarbons exhibit different structural characteristics. For a full monolayer of water, the hydrocarbons are spread across the water, as they are with no water present, and the height of the hydrocarbons equilibrates very quickly (within the standard 0.5 ns at 300 K described in the Methodology). However, as the water concentration was decreased, extended equilibration times were necessary and we see the quick formation of droplets. In both the case of θ_{0,H_2O} = 0.67 and 0.33, the average height of the carbon continually increases over 0.5 ns and doesn't plateau until XXX. Visually inspecting the equilibration process, the hydrocarbons form prominent droplets, where the droplets are more pronounced at θ_{0,H_2O} = 0.33 than at $\theta_{0,H_2O} = 0.67$. When there is less water sitting atop the substrate, there are voids between the hydrocarbons and the substrate, which creates an additional frustration. This frustration ultimately causes the hydrocarbons to layer, phase separate, and form droplets atop the water.

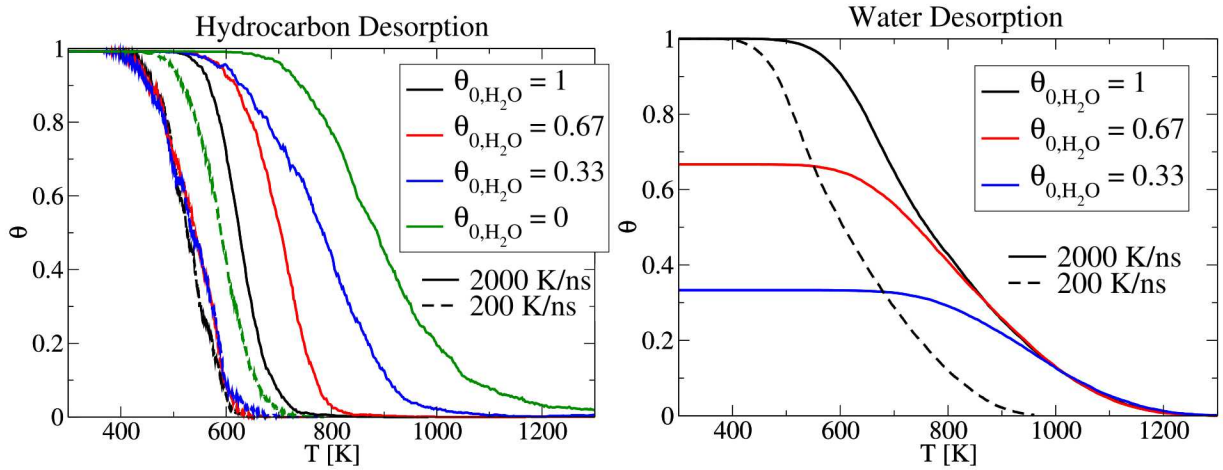

FIGURE 7. Desorption profiles for hydrocarbon-water mixtures with varying water concentration, (black) θ_{0,H_2O} = 1, (red) θ_{0,H_2O} = 0.67, (blue) θ_{0,H_2O} = 0.33, and (green) θ_{0,H_2O} = 0. with different temperature ramp rates; (solid) 2000 K/ns and (dashed) 200 K/ns. The left figure shows the hydrocarbon desorption while the right figure shows the water desorption. The green curve is omitted from the right figure because there is no water in that system. The same color/line-types correspond to the same simulation.

Interestingly, due to this structural difference in the hydrocarbons, we observe fundamental differences in the hydrocarbon desorption curves as a function of temperature ramp rate. When the ramp rate is relatively fast (i.e. 2000 K/ns), the rate of conduction becomes important as the hydrocarbons that are sitting at the top of the phase separated droplets do not feel the heat from the substrate as fast the hydrocarbons closer to the water/substrate. In other words, when the hydrocarbons are more evenly spread over the water (i.e. not in droplets), the heat is distributed more evenly and causes the hydrocarbons to desorb more quickly than when the hydrocarbons form droplets. This is shown at the desorption temperature increases significantly with decreasing water concentration. When the ramp rate is a factor of 10 slower (i.e. 200 K/ns), the conduction through the droplets is less meaningful. The heat from the substrate is able to distribute itself more evenly, whether the hydrocarbons are spread over the surface or in droplets, ultimately leading to minimal differences in the desorption profiles as a function of water concentration. In the case of no water, the green curves in Fig. 7, the temperature desorption is higher than the black, red, or blue curves because the hydrocarbon-substrate interaction is greater than the hydrocarbon-water interaction.

CONCLUSION

In this paper, we analyze the desorption of hydrocarbon and water molecules from an α-Fe_2O_3 (0 0 0 1) substrate. We find that the desorption temperature is minimally different ($< 2\%$) between $C_{24}H_{50}$ paraffin and $C_{24}H_{48}$ naphthene hydrocarbons. Furthermore, the desorption temperature is independent of hydrocarbon coverage. The desorption temperature decreases with increasing hydrocarbon chain length due to the increase van der Waals interactions with increasing number of monomers. When the hydrocarbons are in the presence of water, the water sits directly on top of the iron-oxide surface while the hydrocarbons phase separate on top of the water. In increasing the hydrocarbon

concentration, the water desorption rate decreases on the order of 3.5% from nearly full hydrocarbon coverage ($\theta = 0.992$) and no hydrocarbons. On the contrary, varying the water concentration has a much more significant effect on the hydrocarbon desorption. When the water concentration is below a full monolayer, the voids between the hydrocarbons and substrate cause the hydrocarbons to form droplets atop of the water. This effect is greater when the water coverage is less and there are more voids. When the temperature ramp rate is extremely fast (i.e. 2000 K/ns), the conduction of the heat from the substrate to the water to the hydrocarbons is important depending on the structure of hydrocarbons. When the hydrocarbons are evenly spread over the water, the conduction is more efficient and causes the hydrocarbons to desorb more quickly than when the hydrocarbons are in droplets where the hydrocarbons at the top of the droplet are less hot than the hydrocarbons closer to the substrate. When the temperature rate is slower, the heat is transferred to the hydrocarbons, despite whether the hydrocarbons are evenly distributed over the water or form droplets atop the water, and the water concentration is less important on the overall desorption.

ACKNOWLEDGMENTS

Sandia National Laboratories is a multi-mission laboratory managed and operated by National Technology and Engineering Solutions of Sandia, LLC., a wholly owned subsidiary of Honeywell International, Inc., for the US Department of Energys National Nuclear Security Administration under contract DE-NA0003525.

REFERENCES

1. D. Welch, N. Bennett, T. Genoni, D. Rose, C. Thoma, C. Miller, and W. Stygar, "Electrode contaminant plasma effects in 1 0 7-a z pinch accelerators," Physical Review Accelerators and Beams **22**, 070401 (2019).
2. M. Cuneo, "The effect of electrode contamination, cleaning and conditioning on high-energy pulsed-power device performance," IEEE transactions on dielectrics and electrical insulation **6**, 469–485 (1999).
3. D. Rose, E. Madrid, D. Welch, R. Clark, C. Mostrom, W. Stygar, and M. Cuneo, "Computational analysis of current-loss mechanisms in a post-hole convolute driven by magnetically insulated transmission lines," Physical Review Special Topics-Accelerators and Beams **18**, 030402 (2015).
4. E. Madrid, D. Rose, D. Welch, R. Clark, C. Mostrom, W. Stygar, M. Cuneo, M. Gomez, T. Hughes, T. Pointon, *et al.*, "Steady-state modeling of current loss in a post-hole convolute driven by high power magnetically insulated transmission lines," Physical Review Special Topics-Accelerators and Beams **16**, 120401 (2013).
5. K. Vermöhlen, H. Lewandowski, H.-D. Narres, and E. Koglin, "Adsorption of polyacrylic acid on aluminium oxide: Drift spectroscopy and ab initio calculations," Colloids and Surfaces A: Physicochemical and Engineering Aspects **170**, 181–189 (2000).
6. M.-T. Nguyen, N. Seriani, and R. Gebauer, "Water adsorption and dissociation on α-fe2o3 (0001): Pbe+ u calculations," The Journal of chemical physics **138**, 194709 (2013).
7. P. Dementyev, K.-H. Dostert, F. Ivars-Barceló, C. P. O'Brien, F. Mirabella, S. Schauermann, X. Li, J. Paier, J. Sauer, and H.-J. Freund, "Water interaction with iron oxides," Angewandte Chemie International Edition **54**, 13942–13946 (2015).
8. C. Gattinoni, J. P. Ewen, and D. Dini, "Adsorption of surfactants on α-fe2o3 (0001): A density functional theory study," The Journal of Physical Chemistry C **122**, 20817–20826 (2018).
9. C.-L. Chia, C. Avendaño, F. R. Siperstein, and S. Filip, "Liquid adsorption of organic compounds on hematite α-fe2o3 using reaxff," Langmuir **33**, 11257–11263 (2017).
10. M. Doig, C. P. Warrens, and P. J. Camp, "Structure and friction of stearic acid and oleic acid films adsorbed on iron oxide surfaces in squalane," Langmuir **30**, 186–195 (2013).
11. C. A. Latorre, J. P. Ewen, C. Gattinoni, and D. Dini, "Simulating surfactant-iron oxide interfaces: From density functional theory to molecular dynamics," (2019).
12. A. Jaishankar, A. Jusufi, J. L. Vreeland, S. Deighton, J. Pellettiere, and A. M. Schilowitz, "Adsorption of stearic acid at the iron oxide/oil interface: Theory, experiments, and modeling," Langmuir **35**, 2033–2046 (2019).
13. J. M. D. Lane, K. Leung, A. P. Thompson, and M. E. Cuneo, "Water desorption from rapidly-heated metal oxide surfaces—first principles, molecular dynamics, and the temkin isotherm," Journal of Physics: Condensed Matter **30**, 465002 (2018).
14. R. T. Cygan, J.-J. Liang, and A. G. Kalinichev, "Molecular models of hydroxide, oxyhydroxide, and clay phases and the development of a general force field," The Journal of Physical Chemistry B **108**, 1255–1266 (2004).
15. W. L. Jorgensen, D. S. Maxwell, and J. Tirado-Rives, "Development and testing of the opls all-atom force field on conformational energetics and properties of organic liquids," Journal of the American Chemical Society **118**, 11225–11236 (1996).
16. H. J. Berendsen, J. P. Postma, W. F. van Gunsteren, and J. Hermans, "Interaction models for water in relation to protein hydration," in *Intermolecular forces* (Springer, 1981) pp. 331–342.
17. S. Plimpton, "Fast parallel algorithms for short-range molecular dynamics," Journal of computational physics **117**, 1–19 (1995).
18. S. W. Siu, K. Pluhackova, and R. A. Böckmann, "Optimization of the opls-aa force field for long hydrocarbons," Journal of Chemical Theory and Computation **8**, 1459–1470 (2012).
19. M. Gomez, R. Gilgenbach, M. Cuneo, C. Jennings, R. McBride, E. Waisman, B. Hutsel, W. Stygar, D. Rose, and Y. Maron, "Experimental study of current loss and plasma formation in the z machine post-hole convolute," Physical Review Accelerators and Beams **20**, 010401 (2017).
20. G. S. Parkinson, "Iron oxide surfaces," Surface Science Reports **71**, 272–365 (2016).